Atmospheric turbulence profiling with multi-aperture scintillation of a Shack–Hartmann sensor

Hajime Ogane [ID],[1][*] Masayuki Akiyama [ID],[1] Shin Oya[2] and Yoshito Ono[3]

[1]*Astronomical Institute, Tohoku University, 6-3 Aramaki, Aoba-ku Sendai, Miyagi 980-8578, Japan*
[2]*National Astronomical Observatory of Japan, 2-21-1 Osawa, Mitaka, Tokyo 181-8588, Japan*
[3]*Subaru Telescope, National Astronomical Observatory of Japan, 650 North Aohoku Place Hilo, HI 96720, USA*

ABSTRACT

Adaptive optics (AO) systems that use tomographic estimation of the three-dimensional structure of atmospheric turbulence require the vertical atmospheric turbulence profile, which describes turbulence strength as a function of altitude as prior information. We propose a novel method to reconstruct the profile by applying a multi-aperture scintillation sensor (MASS) method to scintillation data obtained by a Shack–Hartmann wavefront sensor (SH-WFS). Compared with a traditional MASS, which uses atmospheric scintillation within four concentric annular apertures, the new method utilizes scintillation in several hundreds of spatial patterns, which are created by combinations of SH-WFS subapertures. Accuracy of the turbulence profile reconstruction is evaluated with Bayesian inference, and it is confirmed that the turbulence profile with more than 10 layers can be reconstructed because of the large number of constraints. We demonstrate the new method with a SH-WFS attached to the 51-cm telescope at Tohoku University and we confirm that the general characteristics of the atmospheric turbulence profile are reproduced.

Key words: atmospheric effects – instrumentation: adaptive optics – site testing.

1 INTRODUCTION

The fluctuation of the refractive index in the Earth's atmosphere distorts the wavefront or equiphase surface of starlight and causes blurring of the stellar image. Adaptive optics (AO) systems realize diffraction-limited spatial resolution images with ground-based large aperture telescopes. In AO systems, by using a natural guide star (NGS) or an artificial laser guide star (LGS) as a reference source, the distortion of a wavefront is measured by a wavefront sensor (WFS) and corrected by a deformable mirror (DM) in a time-scale of ~1 ms.

In the last decade, in order to improve the performance of AO systems that use a single LGS, which is affected by the cone effect (Tallon & Foy 1990) and angular anisoplanatism (Stone et al. 1994), AO systems using multiple LGSs and WFSs have been demonstrated or developed for the 8-m class of telescopes (e.g. Marchetti et al. 2007; Arsenault et al. 2012; Lardière et al. 2014; Rigaut et al. 2014; Minowa et al. 2017). These systems measure the wavefront distortion in several lines of sight and reconstruct the distortions optimized in the direction of science objects using tomographic estimation, aiming for AO correction of the lower wavefront error, with laser tomography adaptive optics (LTAO), or a wider field of view with multiconjugate adaptive optics (MCAO; Beckers 1988; Rigaut & Neichel 2018), ground-layer adaptive optics (GLAO; Rigaut 2002; Tokovinin 2004), multi-object adaptive optics (MOAO; Hammer et al. 2004; Vidal, Gendron & Rousset 2010). The tomographic turbulence estimation

is essential technique for next-generation giant segmented mirror telescopes (GSMTs), which have 30-m class primary mirrors.

The tomographic estimation of the three-dimensional turbulence structure requires prior information of the strength of atmospheric turbulence as a function of altitude, which is called the atmospheric turbulence profile. A tomographic reconstruction matrix is computed from the positions of guide stars and the vertical atmospheric turbulence profile. Imperfect prior information of the turbulence profile causes tomographic error, which accounts for a large fraction of the total AO error budget (Gilles, Wang & Ellerbroek 2008). Because the atmospheric turbulence profile varies with time, the tomographic reconstruction matrix should be updated in a time-scale of tens of minutes, which corresponds to the typical time-scale of the profile time evolution (Gendron et al. 2014; Farley et al. 2020).

Altitude resolution is an important parameter for atmospheric turbulence profiling to reflect the precise turbulence distribution in the tomographic reconstruction matrix. Fusco & Costille (2010) and Costille & Fusco (2012) studied the effect of the number of layers in the turbulence profile on the tomographic error in the tomographic AO systems of extremely large telescopes. They created a less-resolved turbulence profile by under-sampling the original highly resolved (250 layers, $\Delta h \sim 100$ m) turbulence profile obtained by a balloon experiment and they investigated the impact of the number of layers for reconstruction on the tomographic error. The conclusion is that at least 10–20 layers are needed to achieve a tomographic error comparable with that obtained using a 250-layer profile. The required number of layers depends on the LGS asterism diameter and the tolerated tomographic error and can be reduced by optimizing the altitude combination of the profile or optimized compression method (Saxenhuber et al. 2017; Farley et al. 2020).

[*] E-mail: h.ogane@astr.tohoku.ac.jp

A number of methods have been developed to obtain the real-time atmospheric turbulence profile based on optical triangulation. Scintillation detection and ranging (SCIDAR; Rocca, Roddier & Vernin 1974) uses the spatial correlation of a scintillation map on the pupil plane from two bright stars with an angular separation of several arcseconds. Because the variance of intensity fluctuation is proportional to the apparent altitude with the power of 5/6, SCIDAR does not have sensitivity to turbulence at low altitudes. Generalized-SCIDAR (G-SCIDAR; Avila, Vernin & Masciadri 1997) has overcome this limitation by detecting scintillation on a plane at some distance away from the pupil plane. Slope detection and ranging (SLODAR; Wilson 2002) has the same triangulation principle as SCIDAR but it uses the spatial correlation of a phase map on the pupil plane, and the correlation is sensitive to the ground layer. Because these methods are based on optical triangulation between two stars, these methods can be limited by the availability of double stars. In addition, these methods do not have any sensitivity to turbulence at high altitudes because the spatial correlation length created by the high turbulence layer is larger than the size of the pupil.

The multi-aperture scintillation sensor and differential image motion monitor (MASS-DIMM; Kornilov et al. 2007) is one of the most common profilers, which uses a single star and has lower altitude resolution compared with SLODAR. This is a method that combines the MASS (Tokovinin et al. 2003; Kornilov et al. 2003) and the DIMM (Sarazin & Roddier 1990). The MASS reconstructs a six-layer profile of the free atmosphere based on the scintillation from a single bright star detected by some spatial patterns on the pupil plane. Meanwhile, the DIMM measures total seeing or the Fried parameter based on the variance of differential image motion through two small apertures. Ground-layer seeing is estimated with the difference between the MASS seeing (free-atmosphere seeing) and the DIMM seeing (total seeing). Then, a seven-layer (ground-layer plus six MASS layers) turbulence profile can be obtained.

Recently, in order to improve the altitude resolution of the MASS, fine spatial sampling of scintillation using a fast and low-noise detector has been demonstrated using a full aperture scintillation sensor (FASS; Guesalaga et al. 2016, 2021) method. The FASS measures the angular power spectrum of scintillation on the pupil plane and compares it with simulated spectra to reconstruct a turbulence profile with 14 layers from 0.3 to 25 km above the ground.

In this paper, we propose another new turbulence profiling method, which carries out scintillation measurements similar to the MASS using the spot brightness fluctuation data of a Shack–Hartmann wavefront sensor (SH-WFS). Hereafter, we call this new method SH-MASS. Compared with the traditional MASS instrument, which measures scintillation with four concentric annuli, the SH-WFS can measure the scintillation with many spatial patterns created from combinations of subapertures of the SH-WFS. Because of the larger number of measurements, the SH-MASS approach utilizes more constraints on the turbulence profile than the MASS. These constraints make it possible to estimate the atmospheric turbulence profile with high altitude resolution using observations of the scintillation of a single star. As an additional merit of using the SH-WFS, it is worth noting that the SH-WFS can be combined with the above-mentioned slope-based profiling methods. For example, the DIMM can be conducted using differential image motions of two SH-WFS spots and SLODAR can also be executed simultaneously if two SH-WFSs are available.

This paper is organized as follows. In Section 2, the principle of the MASS is reviewed and the application to the method to SH-WFS data is explained. In Section 3, the response function of SH-MASS is evaluated through simulations with a single layer of turbulence. In Section 4, an on-sky experiment conducted with the 51-cm telescope at Tohoku University is explained and the results of atmospheric profiling are shown. In Section 5, the remaining problems and limitations of SH-MASS are discussed. Finally, we summarize in Section 6.

2 PRINCIPLE

2.1 Review of the principle of the MASS

In this subsection, the principle of the MASS is summarized following Kornilov et al. (2003) and Tokovinin et al. (2003). Let us consider that light with a wavelength of λ passes through a single layer of atmospheric turbulence with altitude h and thickness Δh. The phase of the light is distorted by fluctuation of the refractive index in the turbulence layer according to the turbulence strength, which is indicated by the structural constant of the refractive index fluctuation $C_N^2(h)$. Then, assuming the Kolmogorov atmospheric turbulence model, the spatial power spectrum of the phase fluctuation Φ_ϕ (m^2) is written as

$$\Phi_\phi(f_x, f_y) = 0.38\lambda^{-2} f^{-11/3} C_N^2(h)\Delta h, \tag{1}$$

where f_x and f_y are spatial frequencies and $f = \sqrt{f_x^2 + f_y^2}$. Besides, by assuming the Fresnel propagation, and the weak perturbation (Rytov) approximation, which is applicable for astronomical observations at not very large zenith angle z, the spatial power spectrum of the intensity fluctuation Φ_I (m^2) is written as

$$\Phi_I(f_x, f_y) = 4\sin^2[\pi\lambda h \sec(z)f^2]\Phi_\phi(f_x, f_y). \tag{2}$$

Here, $h\sec(z)$ represents the apparent altitude of the turbulence layer, or light propagation distance from the layer. Generally, multiple turbulence layers at different altitude and thickness affect the intensity fluctuation. The total contribution from these multiple layers can be written as a linear combination of that from each layer,

$$\Phi_I(f_x, f_y) = \sum_i^{N_{\text{layer}}} 1.53 f^{-11/3} \left\{ \frac{\sin[\pi\lambda h_i \sec(z)f^2]}{\lambda} \right\}^2 C_N^2(h_i)\Delta h_i, \tag{3}$$

where N_{layer} is the number of layers and i is the index of each turbulence layer.

Fig. 1 shows the power spectrum of intensity fluctuation. In this plot, $\Phi_I(f_x, f_y)$ in equation (2) integrated at constant f, i.e. $2\pi f\Phi_I(f_x, f_y)$, is shown as a function of f. A single turbulence layer with a constant turbulence strength and monochromatic ($\lambda = 500$ nm) observation is assumed. The spatial frequency at which the power of scintillation has its peak depends on the propagation distance of the turbulence layer. The layer is higher, and the lower spatial frequency accounts for a large amount of the power. Hence, detecting scintillation at different spatial frequencies makes it possible to discern the contributions from turbulence layers at different altitudes. The amplitude of the power of scintillation also depends on the altitude of the turbulence layer, and contributions from lower layers are weaker. Scintillation hardly has the information of turbulence at the ground layer or dome seeing because Φ_I in equation (2) becomes 0 at $h = 0$.

The MASS is used to estimate the turbulence profile by utilizing the dependence of the spatial frequency of the intensity fluctuation on the apparent altitude of the turbulence layer. The MASS instrument divides the pupil into several concentric annuli (see Fig. 2) and measures the starlight intensity in the concentric apertures. The intensity fluctuation is characterized by the scintillation index (SI),
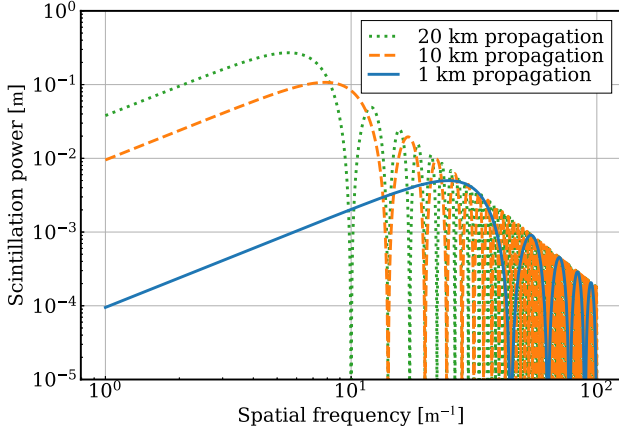
Figure 1. One-dimensional spatial power spectra of scintillation are shown, where the vertical axis shows $\Phi_I(f_x, f_y)$ integrated at constant f; $2\pi f \Phi_I(f_x, f_y)$. The monochromatic ($\lambda = 500$nm) scintillation power spectrum, which is created by a single turbulence layer with a constant turbulence strength ($C_N^2(h)\Delta h = 1.0E - 12[\text{m}^{1/3}]$) at the propagation distances of 1, 10 and 20 km, is shown by blue solid, orange dashed and green dotted lines, respectively.
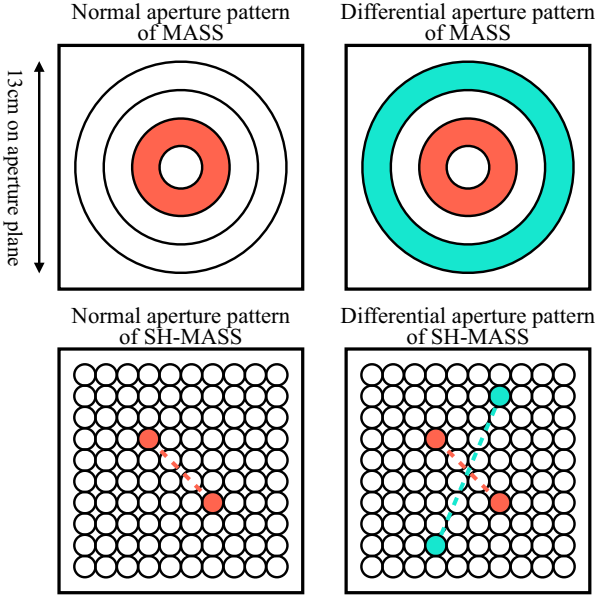

Figure 2. The top panels show examples of MASS spatial patterns whose measurements are used to compute SIs. For example, a normal SI is calculated as the intensity variance measured by a red annular aperture while a differential SI is calculated as the intensity covariance between the measurement by a red aperture and that by a blue aperture. The bottom panels show examples of spatial patterns for SH-MASS. In our definition, a normal SI is calculated as the intensity variance observed by a red subaperture pair while a differential SI is computed as the intensity covariance between the observation by a red subaperture pair and a blue subaperture pair. In the calculation of differential SIs, only two subaperture pairs that have a common mid-point are used.

which is the variance and covariance of the normalized intensity observed by the concentric apertures. Denoting the observed intensity in the Xth annulus as I_X, the intensity variance of the Xth annulus, referred to as the normal scintillation index, is defined as

$$s_X = \text{Var}\left[\frac{I_X}{\langle I_X \rangle}\right], \tag{4}$$

where $\langle\rangle$ represents the time-average, and Var means variance. Likewise, the intensity covariance of the Xth and Yth annuli, referred to as a differential scintillation index, is defined as

$$
\begin{aligned}
s_{XY} &= \text{Var}\left[\frac{I_X}{\langle I_X \rangle} - \frac{I_Y}{\langle I_Y \rangle}\right] \\
&= s_X + s_Y - 2\text{Cov}\left[\frac{I_X}{\langle I_X \rangle}, \frac{I_Y}{\langle I_Y \rangle}\right],
\end{aligned} \tag{5}
$$

where Cov means covariance.

These SIs can be expressed using the power spectrum of intensity fluctuation $\Phi_I(f_x, f_y)$ as follows:

$$s_X = \iint \Phi_I(f_x, f_y)|\mathcal{F}[A_X(x, y)]|^2 \, df_x \, df_y, \tag{6}$$

$$s_{XY} = \iint \Phi_I(f_x, f_y)|\mathcal{F}[A_X(x, y) - A_Y(x, y)]|^2 \, df_x \, df_y, \tag{7}$$

Here, $\mathcal{F}$ means Fourier transformation and $A(x, y)$ is the normalized aperture function; a function that returns a value of 1 divided by the area of the aperture for (x, y) inside the aperture, and a value of 0 otherwise. By substituting equation (3) into $\Phi_I(f_x, f_y)$ in equations (6) and (7), the following formulas are obtained.

$$s_X = \sum_{i}^{N_{\text{layer}}} W_{X,i} J_i, \tag{8}$$

$$s_{XY} = \sum_{i}^{N_{\text{layer}}} W_{XY,i} J_i, \tag{9}$$

where

$$
\begin{aligned}
W_{X,i} = \iint 1.53 f^{-11/3} &\left\{\frac{\sin[\pi\lambda h_i \sec(z) f^2]}{\lambda}\right\}^2 \\
&\times |\mathcal{F}[A_X(x, y)]|^2 \, df_x \, df_y,
\end{aligned} \tag{10}
$$

$$
\begin{aligned}
W_{XY,i} = \iint 1.53 f^{-11/3} &\left\{\frac{\sin[\pi\lambda h_i \sec(z) f^2]}{\lambda}\right\}^2 \\
&\times |\mathcal{F}[A_X(x, y) - A_Y(x, y)]|^2 \, df_x \, df_y,
\end{aligned} \tag{11}
$$

$$J_i = C_N^2(h_i)\Delta h_i. \tag{12}$$

Here, $W_{X,i}$ and $W_{XY,i}$ are called normal weighting functions (WFs) and differential WFs, respectively, and they can be calculated from the information of aperture geometry and measurement wavelength. By solving equations (8) and (9), turbulence strengths $J_i = C_N^2(h_i)\Delta h_i$ of multiple layers are estimated. A typical MASS instrument has four concentric annular apertures whose diameters are 2.0, 3.7, 7.0 and 13.0 cm. Then, ten SIs (four normal SIs plus six differential SIs) are derived in order to reconstruct a turbulence profile of six turbulence layers (0.5, 1, 2, 4, 8 and 16 km above the aperture). Each SI is calculated every minute from the photon counting with ~1 kHz (see Kornilov et al. 2003).

In real measurements, spectral characteristics such as the spectral energy distribution of the observed star, filter transmission characteristics and detector sensitivity need to be considered. According to Tokovinin (2003), the effect from the polychromatic scintillation can be described by replacing the WFs as follows:

$$
\begin{aligned}
W_{X,i} = \iint 1.53 f^{-11/3} &\left\{\int \frac{\sin[\pi\lambda h_i \sec(z) f^2]}{\lambda} F(\lambda) \, d\lambda\right\}^2 \\
&\times |\mathcal{F}[A_X(x, y)]|^2 \, df_x \, df_y,
\end{aligned} \tag{13}
$$

$$W_{XY,i} = \iint 1.53 f^{-11/3} \left\{ \int \frac{\sin[\pi\lambda h_i \sec(z) f^2]}{\lambda} F(\lambda)\,\mathrm{d}\lambda \right\}^2$$
$$\times \, |\mathcal{F}[A_X(x, y) - A_Y(x, y)]|^2 \,\mathrm{d}f_x \,\mathrm{d}f_y. \tag{14}$$

Here, $F(\lambda)$ is the normalized spectral function, which contains all the spectral characteristics mentioned above and is normalized to satisfy $\int_{-\infty}^{\infty} F(\lambda)\,\mathrm{d}\lambda = 1$.

2.2 Application of the MASS to SH-WFS data

Because the SH-WFS effectively divides the entrance pupil into grid pattern subapertures, it can be used to measure scintillation in many spatial patterns by multiple combinations of subapertures. Therefore, the SH-WFS can be applied to the MASS method.

Fig. 2 shows a comparison of the definition of spatial patterns in a traditional MASS (top two panels) and in an SH-MASS (bottom two panels). In the traditional MASS case, concentric annular spatial patterns are used to extract scintillation at a specific frequency that corresponds to the diameter of the annulus. For example, a normal SI is defined as an intensity variance measured by the red annulus in the top-left panel of Fig. 2 while a differential SI is defined as an intensity covariance between the red and blue annuli in the top-right panel of Fig. 2.

However, we define a subaperture pair, which consists of two subapertures, as one spatial pattern of the SH-MASS so that we can effectively extract a certain spatial frequency component of scintillation that is characterized by the distance of the two subapertures. Then, the total intensity of a subaperture pair is used as a measured value to calculate a SI. For example, a normal SI is defined as a fluctuation variance of total intensity measured by the two red subapertures in the bottom-left panel of Fig. 2. Based on this definition of normal SI, equation (4) can be rewritten as

$$
\begin{aligned}
s_X &= \mathrm{Var}\left[\frac{I_X}{\langle I_X \rangle}\right] \\
&= \mathrm{Var}\left[\frac{I_i + I_j}{\langle I_i + I_j \rangle}\right] \\
&= \frac{\mathrm{Var}[I_i] + \mathrm{Var}[I_j] + 2\mathrm{Cov}[I_i, I_j]}{(\langle I_i \rangle + \langle I_j \rangle)^2},
\end{aligned} \tag{15}
$$

where i and j are indices of subapertures that constitute aperture X, and I_i represents spot intensity (or counts) observed in the ith subaperture. Because of the large number of SH-WFS subapertures, there are many subaperture pairs that have a common separation distance. Then, we calculated normal SIs for all subaperture pairs that have a common spatial distance and we regarded the average and standard deviation as a normal SI and its measurement error, respectively.

Likewise, a differential SI is defined as a fluctuation covariance between total intensity measured by the two red subapertures and that measured by the two blue subapertures in the bottom-right panel of Fig. 2. Then, equation (5) can be rewritten as

$$
\begin{aligned}
s_{XY} &= s_X + s_Y - 2\mathrm{Cov}\left[\frac{I_X}{\langle I_X \rangle}, \frac{I_Y}{\langle I_Y \rangle}\right] \\
&= s_X + s_Y - 2\mathrm{Cov}\left[\frac{I_i + I_j}{\langle I_i + I_j \rangle}, \frac{I_k + I_l}{\langle I_k + I_l \rangle}\right] \\
&= s_X + s_Y \\
&\quad - 2\frac{\mathrm{Cov}[I_i, I_k] + \mathrm{Cov}[I_j, I_k] + \mathrm{Cov}[I_i, I_l] + \mathrm{Cov}[I_j, I_l]}{(\langle I_i \rangle + \langle I_j \rangle)(\langle I_k \rangle + \langle I_l \rangle)}
\end{aligned}
$$
$$\tag{16}$$

where i and j are indices of subapertures that constitute aperture X, while k and l denote indices of subapertures for aperture Y. Here, we calculated differential SIs for two subaperture pairs that have a common mid-point. This corresponds to taking concentric two annuli in the traditional MASS. By these definitions of spatial patterns in the SH-MASS, 51 normal SIs and 234 differential SIs are obtained with 10×10 SH-WFS.

Fig. 3 shows a comparison of the WFs of the traditional MASS and SH-MASS, which are calculated assuming the aperture geometries shown in Fig. 2 and a measurement wavelength of 500 nm. Each row of the WF matrix represents the WF of each spatial pattern (i.e. equation 10 or 11). Here, values of WFs are normalized in each row so that the weight value transition in the direction of propagation distance can be easily recognized. In the traditional MASS case, the number of spatial patterns is only ten (four normal plus six differential) and the transition occurs at a longer propagation distance for normal spatial patterns, and at a shorter propagation distance for differential spatial patterns. While the traditional MASS WF has a small number of spatial patterns with a discontinuity at ~10 km, in the SH-MASS case, the number of spatial patterns reaches ~300 and their transition distances are continuous from the ground to 20 km high. This implies that the SH-MASS aperture geometry gives a sufficient number of constraints to estimate a turbulence profile with higher altitude resolution.

2.3 Turbulence profile reconstruction method

The reconstruction of a turbulence profile solves an inverse problem described by equations (8) and (9) with an analytically derived WF matrix for observed SIs. If we simply apply a linear reconstruction without consideration of the parameter range, negative turbulence strength often appears. In order to avoid this situation, Tokovinin et al. (2003) applied the χ^2-minimization with y_i of $J_i = y_i^2$ as a variable, where J_i is the turbulence strength of each layer.

In this study, the turbulence profile and associated uncertainty are evaluated based on Bayesian inference with a Markov chain Monte Carlo (MCMC) method. As a prior function of the MCMC method, we applied a top-hat filter to limit the parameter space, as follows:

$$
P(\boldsymbol{J}) = \begin{cases} 1 & \text{if } -32 < \log J_i \,(\mathrm{m}^{1/3}) < -11 \text{ is satisfied by all } J_i \\ 0 & \text{otherwise} \end{cases}.
$$
$$\tag{17}$$

Here, $\boldsymbol{J}$ is the turbulence profile and the strength range of each turbulence layer, i.e. $-32 < \log J_i \,(\mathrm{m}^{1/3}) < -11$, corresponds to $2.0 \times 10^{-2} < r_0 \,(\mathrm{m}) < 8.0 \times 10^{10}$ in the Fried parameter, assuming a measurement wavelength of 500 nm and zenith direction. It is expected that this parameter range covers the possible turbulence strength of a single layer. As a likelihood function of the MCMC method, we use the probability that the observed SIs are obtained from a Gaussian distribution with a mean of the expected SIs and a standard deviation of observation errors as follows:

$$
L(\boldsymbol{s}|\boldsymbol{J}) = \prod_{m=1}^{M} \left[\frac{1}{\sqrt{2\pi\sigma_m^2}} \exp\left\{ -\frac{[s_m - (W\boldsymbol{J})_m]^2}{2\sigma_m^2} \right\} \right]. \tag{18}
$$

Here, M is the number of spatial patterns, $\boldsymbol{s}$ and σ are SIs and their errors, respectively, W is the WF matrix and $\boldsymbol{J}$ is the turbulence profile. By sampling the multidimensional space of $\boldsymbol{J}$ effectively using the Bayesian inference technique, the strength of turbulence and its error is reconstructed for each layer. The reconstruction procedure was conducted utilizing `emcee`, an MCMC tool for Python.

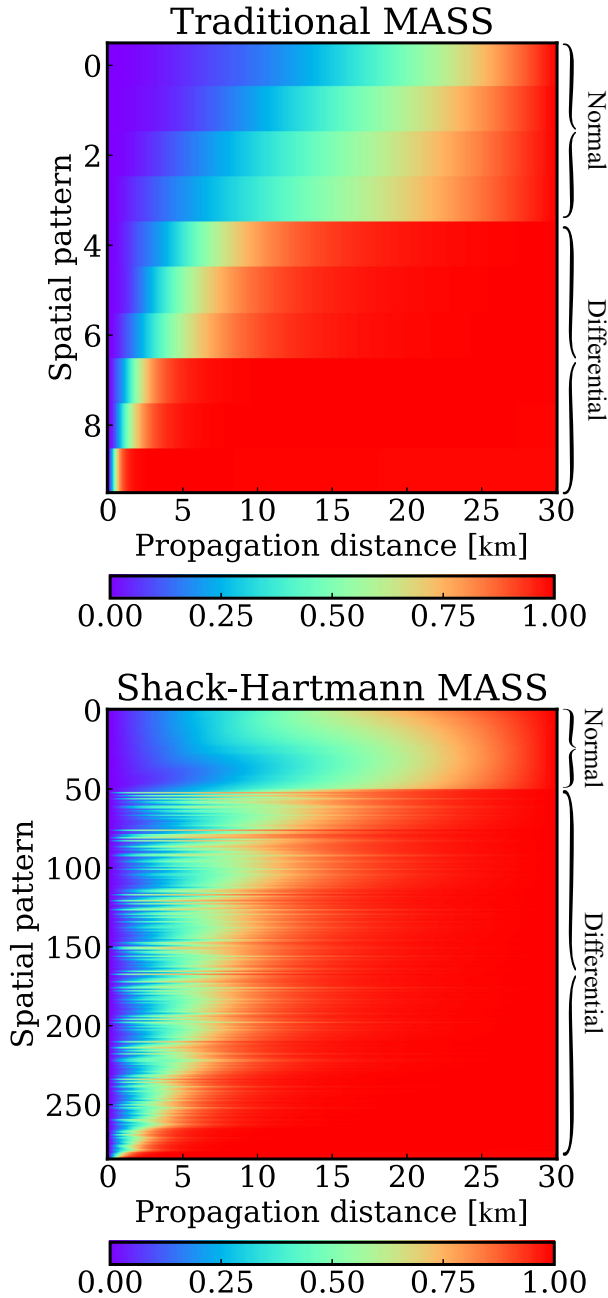## Traditional MASS

Shack-Hartmann MASS

Figure 3. Top: WF matrix of the traditional MASS. Ten spatial patterns are made by four concentric annular apertures whose diameters are 2.0, 3.7, 7.0 and 13.0 cm. Bottom: WF matrix of the SH-MASS. Because of the geometry of the SH-WFS, 10 × 10 subapertures, with each subaperture size scale 1.3 cm on the primary mirror, were assumed. Both WFs are calculated assuming the measured wavelength of 500 nm. Each pixel is coloured with weight value (m$^{-1/3}$) normalized in each row so that the characteristic propagation distance where the weight value reaches the 50th percentile can be seen as light green.

3 PERFORMANCE EVALUATION

3.1 Response function

In order to investigate the SH-MASS's performance of atmospheric turbulence profiling quantitatively, we examine the response of the SH-MASS to a single turbulence layer. In this calculation, at first, we

create a turbulence profile that consists of single turbulence layer at a certain propagation distance. Then, we calculate theoretical SIs by multiplying the WF to the turbulence profile, assuming the measured wavelength of 500 nm. The profiling is conducted with a predefined set of layers. In this study, we select the combinations so that the propagation distance of the lowest layer should be 0.5 km, the propagation distance of the highest layer should be 20.0 km and the ratio of the propagation distance of the nth lowest layer and that of the $(n+1)$th lowest layer should be constant. Finally, the turbulence profile is reconstructed by using the MCMC method described in Section 2.3.

We repeat this procedure by changing the propagation distance of the input single turbulence layer in order to obtain a response function, which is defined as the estimated turbulence strength of each reconstructed layer as a function of propagation distance of the input single turbulence layer. Here, we assume that measurement errors of SIs are 5 per cent of SIs uniformly for all spatial patterns. According to Tokovinin et al. (2003), typical errors of SIs are approximately 2 per cent except for a 3–7 per cent error for the smallest differential SI. The size of the error depends on photon flux. Thus, our assumption of 5 per cent errors would be suitable in order to explore the worst case of a typical performance of the SH-MASS.

In Fig. 4, we compare the response function of the traditional MASS set-up (top panels) and that of the SH-MASS set-up (bottom panels). The assumed spatial pattern for both MASS and SH-MASS are the same as in Figs 2 and 3. Different columns represent different numbers of reconstructed layers. In each panel in Fig. 4, the x-axis represents the propagation distance of the input single turbulence layer while the y-axis represents the ratio of the estimated turbulence strength to the input turbulence strength, and hence the sensitivity of the MASS to a given propagation distance. Each coloured line represents the sensitivity of each reconstructed layer, and errors are defined as the standard deviation of solutions from 10 000 MCMC steps after convergence. Total sensitivity as a sum of the response of all the reconstruction layers is represented by a black dashed line.

By comparing the top and bottom panels in Fig. 4, we can see that the sizes of the estimation errors are smaller in the SH-MASS. In addition, the triangular shape of the SH-MASS response function is kept even with the number of reconstructed layers of 10, while the triangular shape is broken and the altitude resolution is poorer in the traditional MASS case. The black dashed lines are also closer to unity in the SH-MASS cases, which means that the estimation of integrated turbulence strength is improved. These results indicate that a large number of spatial patterns realized by SH-WFS subaperture geometry is effective in reconstructing turbulence profiles with high altitude resolution and sufficient accuracy.

Figs 5 and 6 show how the shape of the response function changes if parameters of the SH-WFS are changed. In Fig. 5, the size of subaperture is varied: cases with diameters of 1.3, 2.0 and 3.0 cm are shown in the top, middle and bottom panels, respectively. Here, the format of the SH-WFS is fixed to 10 × 10 in all cases. If the size of subaperture is increased, the fine spatial structure of scintillation is no longer detectable. Then, scintillation data do not have any information of turbulence at short propagation distances, which is associated with a high spatial frequency scintillation pattern. For this reason, the propagation distance of the lowest reconstructed layer is changed so that the propagation distance $h_1 \sec(z)$ and the size of subaperture x_{subap} satisfy $x_{\mathrm{subap}} \sim \sqrt{\lambda h_1 \sec(z)}$, while the propagation distance of the highest reconstructed layer is fixed to $\sim$20 km. These figures indicate that the size of subaperture is one of the most important parameters of the SH-MASS, which determines the dynamic range of the turbulence profiling. Although the SH-MASS
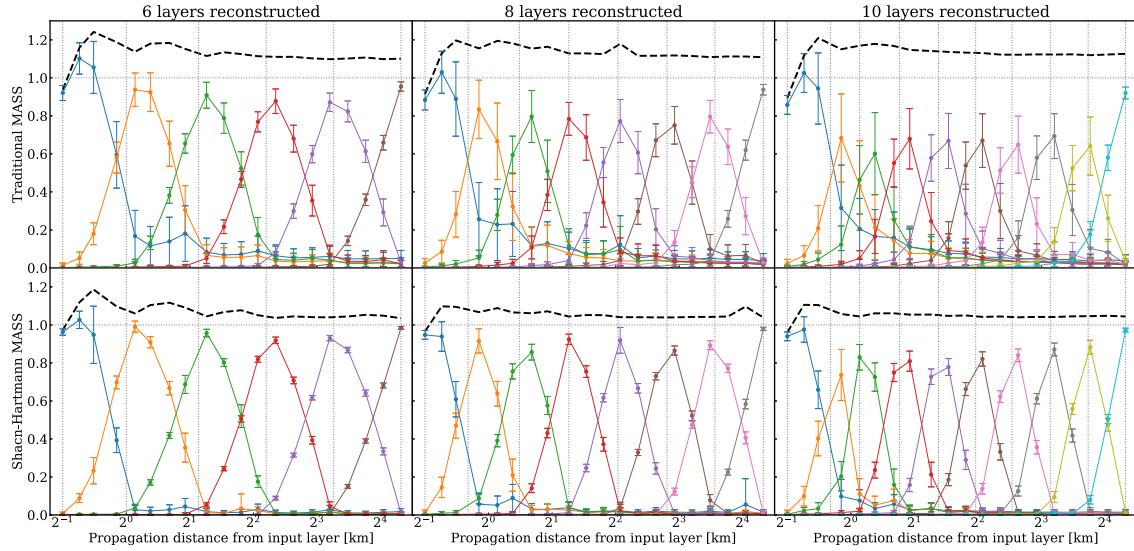
Figure 4. Top panels: The response function for the traditional MASS set-up in which turbulence strengths of 6, 8 and 10 layers are reconstructed using scintillation data observed by four concentric annular apertures. Bottom panels: The response function for a classical SH-MASS set-up in which turbulence strengths of 6, 8 and 10 layers are reconstructed using scintillation data observed by a 10 x 10 SH-WFS whose subaperture diameter corresponds to 1.3 cm on the primary mirror. In each panel, each triangular line represents the response of each reconstruction layer to the input single turbulence layer. When 6, 8 and 10 layers are reconstructed, the propagation distances from the reconstruction layers are [0.5, 1.0, 2.2, 4.6, 9.6, 20.0] km, [0.5, 0.8, 1.4, 2.4, 4.1, 7.0, 11.8, 20.0] km and [0.5, 0.8, 1.1, 1.7, 2.6, 3.9, 5.8, 8.8, 13.3, 20.0] km, respectively. The black dashed line represents the total sensitivity as a sum of the response of all the reconstruction layers. Grey vertical lines denote the propagation distance from the reconstructed layers, while grey horizontal lines denote the sensitivity when all input turbulence strengths are sensed.
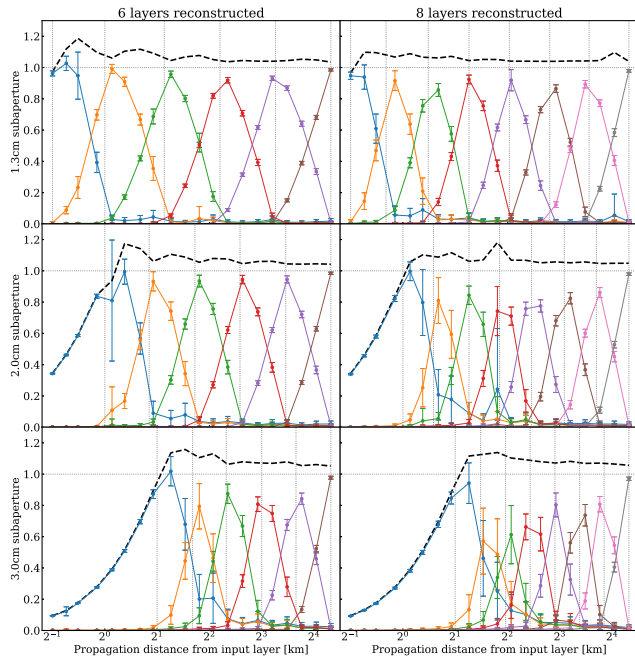

Figure 5. Comparison of the SH-MASS response function for the subaperture diameters of 1.3 cm (top), 2.0 cm (middle) and 3.0 cm (bottom) in the case of 6 (left) and 8 (right) reconstructed layers. Here, the format of the SH-WFS is 10 × 10 for all cases. The propagation distance from the lowest reconstruction layer is changed to 1 and 2 km for the subaperture sizes of 2 and 3 cm, respectively.

Figure 6. Comparison of the SH-MASS response function for the SH-WFS formats of 5 × 5 (top), 10 × 10 (middle) and 15 × 15 (bottom) in the cases of 6 (left) and 8 (right) reconstructed layers. Here, the diameter of the SH-WFS subaperture is 1.3 cm for all cases.

with small subapertures makes it possible to estimate atmospheric turbulence close to the ground, a small subaperture can suffer from the problem of a small number of photons. The diameter of a subaperture should be determined carefully, considering the altitude
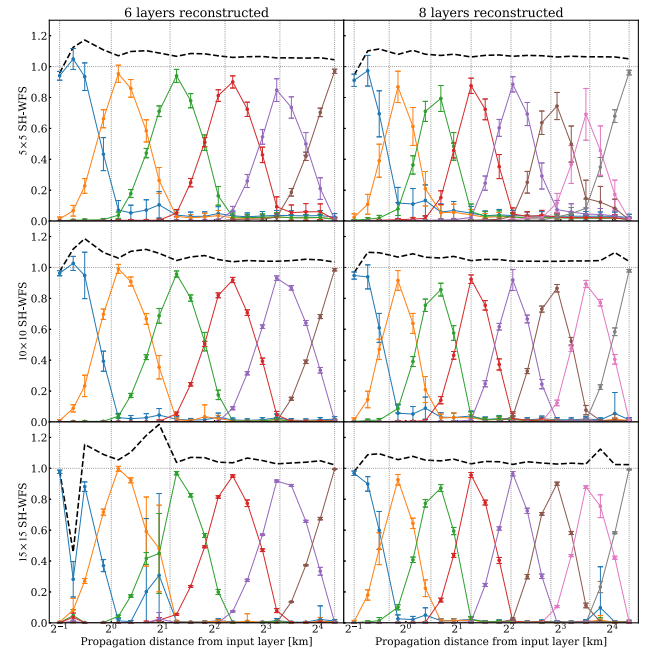
range of estimation, the magnitude of the available star and the availability of a highly sensitive detector with a high pixel readout rate, such as an electron multiplying CCD (EM-CCD).

In Fig. 6, the format of the SH-WFS is varied: 5 × 5, 10 × 10 and 15 × 15 cases are shown in the top, middle and bottom panels, respectively. Here, the diameter of the subaperture is fixed to 1.3 cm

in all cases. It is clear that the size of error becomes smaller if the format of the SH-WFS is larger. This is because of the large number of constraints realized by the larger format. The number of constraints is 43 (15 normals + 28 differentials), 285 (51 normals + 234 differentials), and 1740 (106 normals + 1634 differentials) for 5×5, 10×10 and 15×15 SH-WFS, respectively. However, in the 15×15 case, the MCMC solver does not converge well in some calculations. This would be because too many constraints result in a complicated posterior probability distribution and cause poor convergence in Monte Carlo sampling. Considering the results and computational cost, the format of 10×10 is a suitable size for the SH-WFS.

3.2 Required signal-to-noise ratio

We investigate the required signal-to-noise ratio (S/N) in order to conduct the SH-MASS by simulating scintillation observations using the Monte Carlo method. In our calculation, we assume one subaperture of SH-WFS with the diameter of 2.0 cm attached to a general telescope and WFS system whose total optical transmission is assumed to be ~ 40 per cent. We use a bandpass of combined V and R bands for photons from a star and background sky assuming a certain magnitude of star and sky brightness of $m_{V,\mathrm{sky}} = 21.1$ mag arcsec^{-2} and $m_{R,\mathrm{sky}} = 20.6$ mag arcsec^{-2}, respectively. Here, the number of photons are changed stochastically so that it should follow a Poisson distribution. Additionally, in the stellar photon case, the effect from scintillation is also considered. Assuming SI observed by the subaperture that takes a value of 0.2, 0.5 or 1.0, we randomly vary the number of stellar photons following a lognormal distribution (Zhu & Kahn 2002). For the readout noise of the detector, we assume a stochastic variable that follows a Gaussian distribution with the standard deviation of 1.5 ADU pixel^{-1}. The exposure time is fixed to 2 ms and n is the number of photon countings, taken from 3000, 30 000 or 300 000 times, which corresponds to 6 s, 1 min and 10 min, respectively. After n photon countings, we calculate the observed SI and S/N using the series. The definitions of the SI and S/N in this calculation are

$$\mathrm{SI} = \frac{\mathrm{Var}[n_{\mathrm{star}}]}{\langle n_{\mathrm{star}} \rangle^2}, \tag{19}$$

$$\mathrm{S/N} = \frac{\langle n_{\mathrm{star}} \rangle}{\sqrt{\langle n_{\mathrm{star}} \rangle + \mathrm{Var}[n_{\mathrm{sky}}] + \mathrm{Var}[n_{\mathrm{ron}}]}}, \tag{20}$$

where $\langle n_{\mathrm{star}} \rangle$ and $\mathrm{Var}[n_{\mathrm{star}}]$ are the average and variance of the count from a simulated star, respectively, $\mathrm{Var}[n_{\mathrm{sky}}]$ is the variance of the count from the background sky and $\mathrm{Var}[n_{\mathrm{ron}}]$ is variance of the count from readout noise. We repeat this Monte Carlo simulation of SI and S/N 100 times, and evaluate the dispersion of the SIs.

Fig. 7 shows the ratio of the standard deviation of the 100 SIs to the average of the 100 SIs as a function of S/N. In this plot, the number of photon countings is fixed to 30 000. Hence, a 1-min observation for measuring SI is simulated here. Lines with different colours correspond to different input SIs, and we can see how the SI measurement error decreases when the magnitude of the observed star increases depending on the strength of atmospheric turbulence. The curves become flat at S/N > 3 and the saturated value depends on the input SI. Even at the strong turbulence condition of SI = 1.0, the saturated value is less than 5 per cent, which means that a 1-min observation with S/N > 3 is long enough to achieve sufficient S/N assumed in the calculation of the response functions in Section 3.1.

However, Fig. 8 shows the results with changing n value and a fixed input SI of 0.5. In this plot also, the ratio of the standard deviation
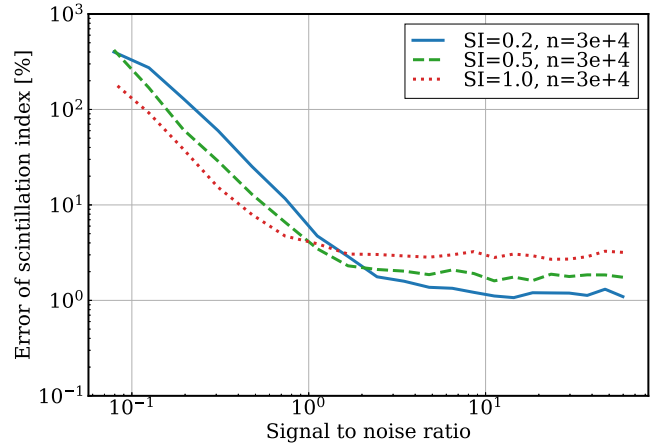

Figure 7. The SI measurement error (the ratio of the standard deviation to the average of 100 measured SIs) as a function of the measured S/N. Lines of different colour denote different input SIs. As the S/N increases, the SI measurement error decreases and saturates to a certain value, which correlates with the real SI value. The saturation occurs at around S/N > 3, which would be the required S/N value for an accurate SI measurement.
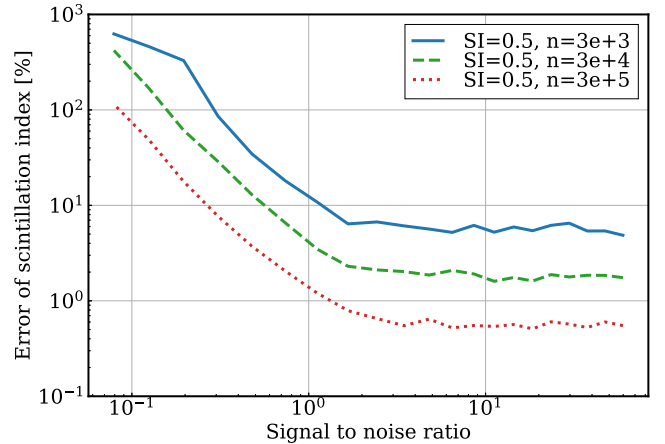

Figure 8. Same as Fig. 7, but lines with different colours denote different numbers of photon counting. As S/N increases, the SI error decreases and saturates to a certain value, which anticorrelates with the number of photon countings. The saturation occurs at S/N > 3, which would be the required S/N value for accurate SI measurement.

to the average of 100 measured SIs become saturated at S/N higher than ~ 3. The saturated value depends on how many frames are used to estimate the SI. This is just because more samples make it possible to estimate the properties of the SI more accurately. Although more frames make it possible to measure the SI with lower measurement error, these frames should be obtained within the characteristic time-scale of atmospheric structure evolution. Considering that the typical time-scale is ~ 10 min and taking into account the result of Fig. 7, $n = 30\,000$ (1 min at 500 Hz) will be the optimal number for scintillation measurements.

4 ON-SKY EXPERIMENT

4.1 Set-up and observation

In order to demonstrate the SH-MASS, we conducted a scintillation observation using a WFS system attached to the 51-cm telescope, IK-
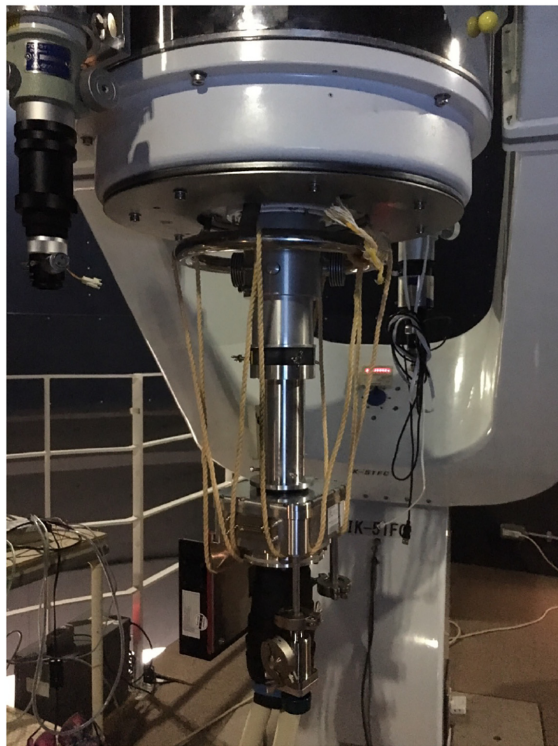
Figure 9. The SH-WFS system attached to the 51-cm telescope at Tohoku University. A lenslet array is in the aluminium cylindrical tube at the centre of the figure. The dewar attached to the tube is an EM-CCD camera. The camera is cooled down using a Peltier device and a liquid cooling system.

51FC at Tohoku University (see Fig. 9). Our WFS system consists of: a collimator; a Bessel *R*-band filter, whose central wavelength is 630 nm; a 150-µm pitch lenslet array (Thorlabs, MLA150-5C) which has a chromium mask for blocking light that reaches outside the circular aperture of each microlens; relay lenses; an EM-CCD camera with an E2V CCD60 128 × 128 24-µm pixel detector; and custom-made readout electronics provided by Nuvu cameras. The primary mirror of the 51-cm telescope is effectively divided into 20 × 20 by the lenslet array; in other words, the effective diameter of a subaperture corresponds to 2.5 cm on the primary mirror. The field of view of each subaperture is ∼35 arcsec. The detector was cooled down to −30 °C so that dark current noise is negligible. One pixel of the detector corresponds to 4.9 arcsec on the sky. An amplification signal of 42.6 V is applied to achieve a factor 300 multiplication gain of the EMCCD. High-speed imaging of 500 Hz was repeated 30 000 times targeting Deneb ($m_R = 1.14$ mag). This procedure was repeated nine times in 1 h on a clear night, 2019 October 16, in Japan Standard Time. In this hour, the elevation of the star changed from 46° to 34°.

4.2 Data analysis

The first step is the measurement of the count value of each SH-WFS spot in each frame. The spot reference frame is created by averaging the 30 000 frames in each data set, and the spot size and locations of spots are measured. By fitting each spot of the reference frame with a Gaussian function, the diameter of the Airy disc is measured to be 4.45 pixels (FWHM is 1.88 pixels). Then, for each frame, we define the inside of circles with a centre of each spot location and a diameter of 5.0 pixels as the spot region, and others as the
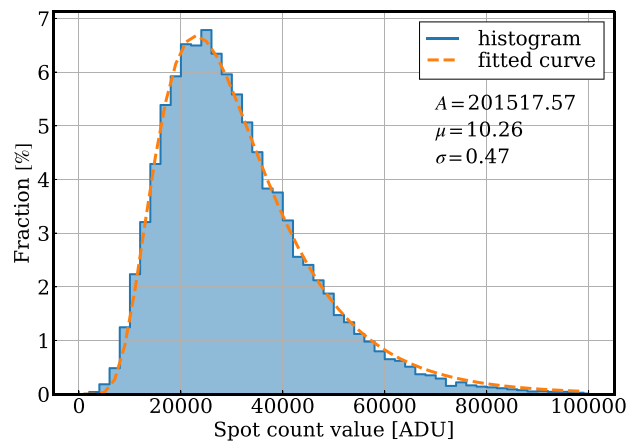

Figure 10. Histogram of count values of one spot of the SH-WFS measured with 500 Hz in 1 min. The horizontal axis represents photon counts after multiplication by the EM-CCD. The distribution is well fitted by a lognormal distribution, which implies that the detected intensity fluctuation is scintillation.

background region. The background count is estimated as the mean count of the background region. After background subtraction from all the pixels, each spot count is calculated as the total counts of each circle in the spot region. Using this procedure, background-subtracted spot counts are calculated for all the spots in the 30 000 frames.

The count fluctuation seen in the 30 000 frames is ascribed to photon noise and atmospheric scintillation. Variance of the fluctuation contributed from photon noise is the mean photon count, while that contributed from scintillation is proportional to the square of the mean photon count. Therefore, considering the observed photon count of ∼100, contribution from scintillation is the dominant component. According to Zhu & Kahn (2002), the distribution of light intensity induced by scintillation follows a lognormal distribution. Then, we check if the histograms of spot counts follow a lognormal distribution written as

$$f(x) = \frac{A}{\sqrt{2\pi}\sigma x} \exp\left[\frac{(\ln x - \mu)^2}{2\sigma^2}\right], \tag{21}$$

where μ and σ are shape parameters of the distribution and A is a normalization parameter. Fig. 10 shows the histogram of count values of a spot in 1 min. The histogram is well fitted by a lognormal distribution function with parameters of $A = 2.0 \times 10^5$, $\mu = 10.26$ and $\sigma = 0.47$. All other spots also follow a similar shape of the histogram, which supports the fact that the observed intensity fluctuation of SH-WFS spots are caused by atmospheric turbulence. However, it should be noted that the lognormal distribution of the count values is not a sufficient condition for concluding that the fluctuation is due to the scintillation.

Then, SIs of all the spatial patterns are calculated from the count fluctuations of spots. The mean, variance and covariance of each spot's count fluctuation are computed and SIs are calculated following equations (15) and (16).

Finally, effects from the finite exposure time are corrected. In this observation, the images are obtained with 2-ms exposure, which means that fluctuation components that have a time-scale of less than 4 ms are smoothed out. Therefore, real SIs that can ideally be observed by a 0-ms exposure time should be larger than those measured by the above-mentioned procedure. In this study, we follow the method described in Tokovinin et al. (2003) in which 0-ms SIs
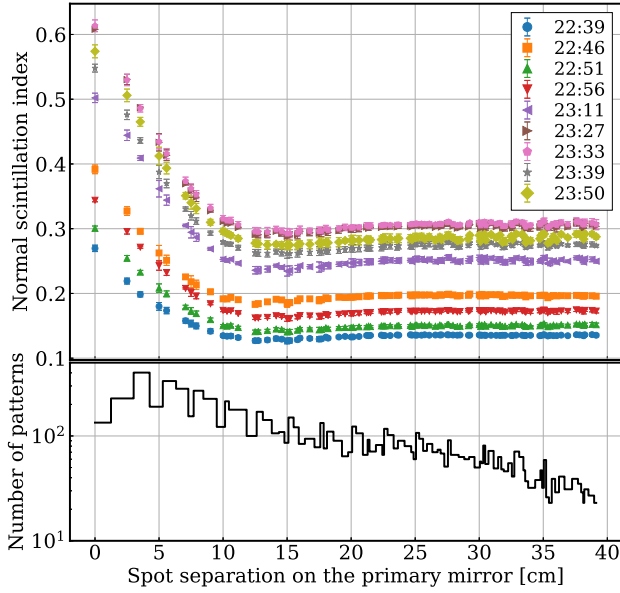
Figure 11. The top panel shows the observed normal SIs, plotted as a function of the separation distance of two subapertures, which constitutes a spatial pattern. Different colours represent different observation times. The values of SIs decrease and become flattened as the separation increases, which indicates that the typical correlation length of scintillation is shorter than 15 cm. Also, the trend that SIs become larger as time goes by can be explained by the variation of the elevation angle of the star. The bottom panel shows the number of subaperture pairs that have a common separation distance. The normal SIs and their errors in the top panel have been calculated as the mean and standard deviation of these numbers of statistics.

are estimated from linear extrapolation of SIs measured by τ-ms exposure and that measured by 2τ-ms exposure:

$$s_0 = 2s_\tau - s_{2\tau}. \tag{22}$$

Here, the data with 2τ-ms exposure are effectively obtained by averaging two adjacent images in the data with τ-ms exposure.

The top panel of Fig. 11 shows the observed normal SIs as a function of separation of two subapertures, which constitutes a normal spatial pattern. Each colour in the plots represents the difference of observed time. The error on each normal SI is small enough to discern the difference between each scintillation state of each observation time. The bottom panel of Fig. 11 shows the number of subaperture pairs that have a common spatial pattern. At all observation times, the normal SI decreases as a function of subaperture separation and is flattened at a spatial length of 10–15 cm and longer. This feature reflects that there is little atmospheric turbulence at higher than $\sim$20 km. In fact, the spatial scale of 10–15 cm is consistent with the typical spatial scale of scintillation created by a turbulence layer; that is, $\sqrt{\lambda h \sec(z)} \sim 13.4$ cm with the assumption of wavelength $\lambda \sim 600$ nm, altitude $h \sim 20$ km and airmass $\sec(z) \sim 1.5$. In addition, this feature can be understood using equation (15). For the null separation case, $\mathrm{Cov}[I_i, I_j]$ becomes $\mathrm{Var}[I_i]$ and SI becomes $\mathrm{Var}[I_i]/\langle I_i \rangle^2$, whereas for the very long separation case, $\mathrm{Cov}[I_i, I_j]$ becomes 0 and SI becomes $\mathrm{Var}[I_i]/2\langle I_i \rangle^2$, half of the SI for the null separation case. Actually, in Fig. 11, the normal SI for a separation longer than 15 cm is almost half of the normal SI for 0-cm separation. Besides, there is a trend that the value of SI becomes larger as time goes by. This can be explained by the change of the elevation of the star. As the elevation becomes lower, the apparent altitude of the turbulence layer becomes higher. Both
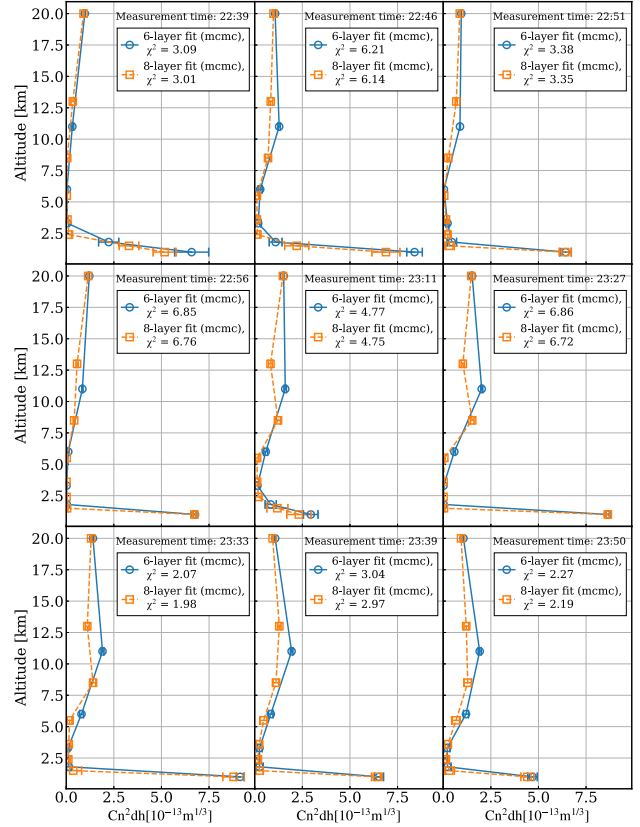

Figure 12. The atmospheric turbulence profile reconstructed by SIs measured at Tohoku University. These profiles are reconstructed using the MCMC estimation method mentioned in Section 2.3. The effect of the elevation angle of the star is corrected. Different panels correspond to different observation times, as described in the title of each panel. Blue lines are profiles that are reconstructed assuming six layers while orange lines assume eight layers. The reduced χ^2 values of each profile estimation are shown in the legends.

effects account for the increase of SIs. These properties also support the fact that the detected fluctuation of stellar intensity is due to the atmospheric turbulence.

4.3 Atmospheric turbulence profile

Fig. 12 shows the atmospheric turbulence profile reconstructed from the observed SIs by the MCMC estimation method described in Section 2.3. Different panels correspond to different observation times, as described in the title of each panel. The propagation distances of reconstructed layers are varied so that the reconstruction altitudes of the layers should be same for all observation times. Blue lines are profiles that are estimated assuming six layers (altitudes of 1.0, 1.8, 3.3, 6.0, 11.0 and 20.0 km above the telescope aperture) while orange lines assume eight layers (altitudes of 1.0, 1.5, 2.4, 3.6, 5.5, 8.5, 13.0 and 20.0 km above the telescope aperture). The reduced χ^2 values, which are less than 10 in all data sets, and the small uncertainties, which represent 1σ values of turbulence strengths after MCMC convergence, imply that the observed normal and differential SIs are described well by the scintillation model. In addition, the overall shape of the profiles shows that the strongest turbulence exists at the lowest layers and the second strongest peak distributes at roughly 10 km. The profiles are consistent with that expected from typical characteristics of the Earth's atmosphere, such as the ground turbulent layer and the tropopause.

5 DISCUSSION

5.1 Fast profile reconstruction using the iterative method

Although the MCMC-based profile estimation method enables us to evaluate the estimation error, it has large calculation costs, and it typically takes a few tens of minutes for a six-layer reconstruction with eight-core parallel processing using an Intel® Core™ i7-4790K CPU and it depends greatly on the number of reconstructed layers. However, the atmospheric turbulence profile as prior information for a tomographic reconstruction matrix has to be updated in a time-scale of tens of minutes. Thus, we try a faster profile calculation based on the Broyden–Fletcher–Goldfarb–Shanno (BFGS) algorithm, which is an iterative solver for the non-linear optimization problem. This algorithm can be utilized with the `scipy.optimize.minimize` module for Python. We impose the same condition of $-32 < \log J_i$ $(\mathrm{m}^{1/3}) < -11$ for all the components of $\mathbf{J}$ as for the MCMC-based method, and we minimize the χ^2 function directly.

However, in the iterative calculation method, the solution is not necessarily the global minimum. Actually, in the current case, a one-time iterative calculation does not give an identical solution. Hence, we conduct the BFGS algorithm 1000 times from 1000 different random initial turbulence profiles. Then, we pick out 100 final turbulence profiles whose χ^2 values are the smallest and we calculate the mean and standard deviation of the 100 profiles.

In Fig. 13, we compare the turbulence profile obtained by the BFGS iterative method with that obtained by the MCMC method. For all observation times, both estimation methods reproduce the same turbulence profile. The consistency suggests that the 1000-time iterative minimization from the random initial profiles is sufficient to find the global minimum. Because the calculation time for the 1000-time iterative minimization is typically a few minutes, the iterative BFGS method can be used for a faster profile reconstruction. Then, we conduct the profile estimation with 10 layers (1.0, 1.4, 1.9, 2.7, 3.8, 5.3, 7.4, 10.3, 14.3 and 20.0 km), which takes a time-scale of days when the MCMC-based method is used. The result is shown in Fig. 14. Here, a higher altitude resolution with dh/h = 1.4 (dh/h = 2.0 for the traditional MASS) is realized for atmospheric turbulence that distributes from 1.0 to 20.0 km. By increasing the number of reconstruction layers, it turns out that the strong turbulence seen at 11.0 km in the six-layer fitting result consists of turbulent layers that distribute at extended altitudes around 7.5–15 km. A precise understanding of the turbulence distribution realized by the high altitude resolution is necessary to produce a realistic reconstruction matrix.

5.2 Low sensitivity to lower altitude

As mentioned in previous works (e.g. Avila et al. 1997), turbulence at less than several hundred metres is undetectable by scintillation-based profiling methods. This is because the variance of observed intensity, or scintillation, is proportional to the propagation distance with a power of 5/6. This characteristic can be seen in our results for the response function (Figs 4, 5 and 6) in which the estimation error of turbulence strength becomes larger for shorter propagation distances of the input layer. In order to overcome this limitation, three solutions can be considered as future improvement plans. The first is the generalized mode: like G-SCIDAR, turbulence at low altitude can be measured by placing the SH-WFS at some distance away from the pupil's plane. The second is the DIMM mode, in which two image motions of a single bright star are measured by two apertures whose centre separation is typically 20–30 cm. By using SH-WFS spots, a star's image motion is observed at various separation lengths.
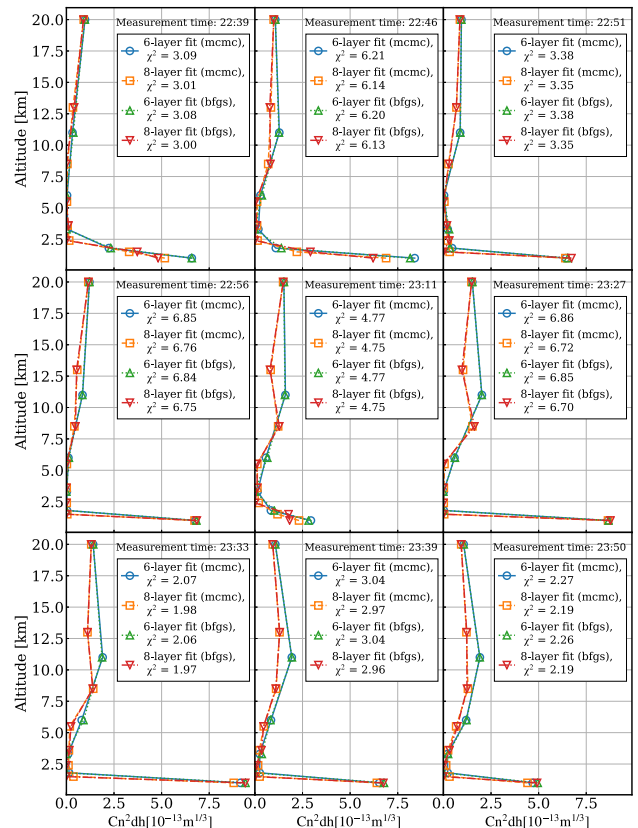

Figure 13. Comparison of the atmospheric turbulence profiles reconstructed by the MCMC-based method (blue and orange lines) and the iterative method (green and red lines). The effect of the elevation angle of the star is corrected. It can be understood that the iterative method reproduces the same profile as the MCMC method. Different panels correspond to different observation times, as described in the title of each panel. The reduced χ^2 values of the solutions from each method are shown in the legends.

Therefore, the DIMM can use the SH-WFS system and the turbulence strength at the ground layer can be estimated by the difference between the DIMM and MASS measurements. The third solution is a combination using SLODAR, which uses two SH-WFSs to measure the correlation of the wavefront distortion from a double star. Because a triangulation-based profiler such as SLODAR does not have any sensitivity to turbulence at high altitude, some SLODAR systems are optimized for profiling of the ground layer (Butterley et al. 2020). Combining SH-MASS with SLODAR enables us to profile the whole atmospheric turbulence using a single optical system.

6 SUMMARY

In this study, we investigate a new MASS-based atmospheric turbulence profiling method called SH-MASS, which reproduces the profile from scintillation observed by a SH-WFS. By evaluating the response functions of the SH-MASS in comparison with those of the traditional MASS, it is shown that SH-MASS theoretically has a higher altitude resolution than the traditional MASS under the assumption that the scintillation measurements have an error of 5 per cent. This high altitude resolution is enabled by the large number of spatial patterns realized by the grid pattern of the SH-WFS.

By investigating the behaviour of response functions by changing the parameters of the SH-MASS, the larger size of subapertures means lower sensitivity to low altitude turbulence. Therefore, a
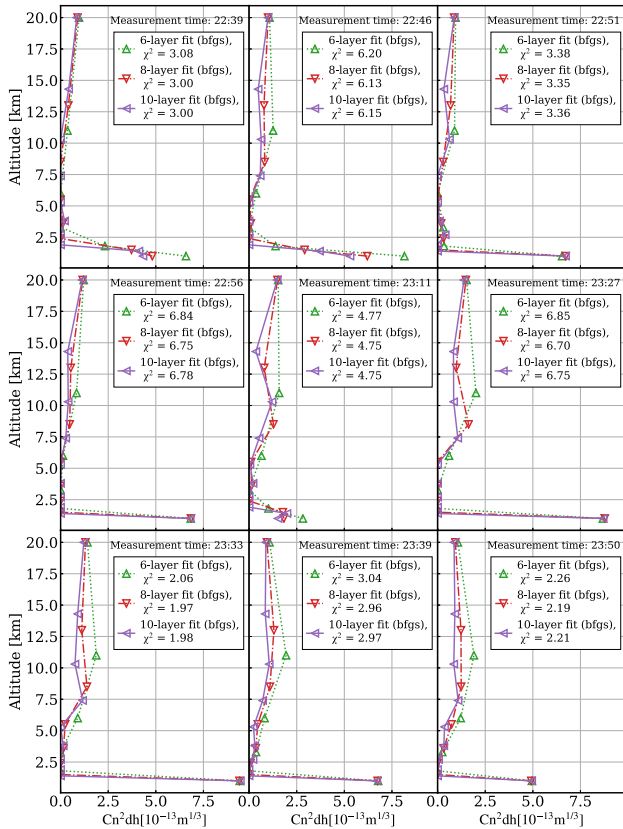
Figure 14. Atmospheric turbulence profiles at Tohoku University. These profiles are reconstructed from the observed SIs using the iterative estimation method mentioned in Section 5.1. The effect of the elevation angle of the star is corrected. Different panels correspond to different observation times, as described in the title of each panel. Green, red and purple lines are profiles reconstructed assuming six, eight and ten reconstructed layers, respectively. The reduced χ^2 values of each profile estimation are described in the legends.

smaller size of subapertures is better as long as the S/N of each spot in a SH-WFS image is larger than ~3.

This new profiler is demonstrated with the 51-cm telescope at Tohoku University and typical characteristics of the atmospheric turbulence are reproduced as the estimated turbulence profile. In order to decrease the calculation costs and to meet the real-time requirement of the profiling (i.e. one profile estimation for ~10 min), we confirm that the faster iterative method can also reproduce the same profile as the MCMC-based method.

DATA AVAILABILITY

The data underlying this article will be shared on reasonable request to the corresponding author.

REFERENCES

Arsenault R. et al., 2012, in Ellerbroek B. L., Marchetti E., Véran J.-P., eds, Proc. SPIE Conf. Ser. Vol. 8447, Adaptive Optics Systems III. SPIE, Bellingham, p. 84470J

Avila R., Vernin J., Masciadri E., 1997, Applied Optics, 36, 7898

Beckers J. M., 1988, in Ulrich M.-H., ed., European Southern Observatory Conference and Workshop Proceedings. ESO, Garching, p. 693

Butterley T., Wilson R., Sarazin M., Dubbeldam C., Osborn J., Clark P., 2020, MNRAS, 492, 934

Costille A., Fusco T., 2012, in Ellerbroek B. L., Marchetti E., Véran J.-P., eds, Proc. SPIE Conf. Ser. Vol. 8447, Adaptive Optics Systems III. SPIE, Bellingham, p. 844757

Farley O., Osborn J., Morris T., Fusco T., Neichel B., Correia C., Wilson R., 2020, MNRAS, 494, 2773

Fusco T., Costille A., 2010, in Ellerbroek B. L., Hart M., Hubin N., Wizinowich P. L., eds, Proc. SPIE Conf. Ser. Vol. 7736, Adaptive Optics Systems II. SPIE, Bellingham, p. 77360J

Gendron E., Morel C., Osborn J., Martin O., Gratadour D., Vidal F., Le Louarn M., Rousset G., 2014, in Marchetti E., Close L. M., Véran J.-P., eds, Proc. SPIE Conf. Ser. Vol 9148, Adaptive Optics Systems IV. SPIE, Bellingham, p. 91484N

Gilles L., Wang L., Ellerbroek B., 2008, in Hubin N., Max C. E., Hubin P. L., eds, Proc. SPIE Conf. Ser. Vol. 7015, Adaptive Optics Systems. SPIE, Bellingham, p. 701520

Guesalaga A., Perera S., Osborn J., Sarazin M., Neichel B., Wilson R., 2016, in Marchetti E., Close L. M., Véran J.-P., eds, Proc. SPIE Conf. Ser. Vol. 9909, Adaptive Optics Systems V. SPIE, Bellingham, p. 99090H

Guesalaga A., Ayancán B., Sarazin M., Wilson R., Perera S., Le Louarn M., 2021, MNRAS, 501, 3030

Hammer F. et al., 2004, Proc. SPIE, 5382, 727

Kornilov V., Tokovinin A. A., Vozyakova O., Zaitsev A., Shatsky N., Potanin S. F., Sarazin M. S., 2003, in Wizinowich P. L., Bonaccini D., eds, Proc. SPIE Conf. Ser. Vol. 4839, Adaptive Optical System Technologies II. SPIE, Bellingham, p. 837

Kornilov V., Tokovinin A., Shatsky N., Voziakova O., Potanin S., Safonov B., 2007, MNRAS, 382, 1268

Lardière O. et al., 2014, in Marchetti E., Close L. M., Véran J.-P., eds, Proc. SPIE Conf. Ser. Vol 9148, Adaptive Optics Systems IV. SPIE, Bellingham, p. 91481G

Marchetti E. et al., 2007, The Messenger, 129, 8

Minowa Y. et al., 2017, in Adaptive Optics for Extremely Large Telescopes V (AO4ELT5). Instituto de Astrofísica de Canarias, Tenerife

Rigaut F., 2002, in Vernet E., Ragazzoni R., Esposito S., Hubin N., eds, European Southern Observatory Conference and Workshop Proceedings, Beyond Conventional Adaptive Optics, Vol. 58. ESO, Garching, p. 11

Rigaut F., Neichel B., 2018, ARA&A, 56, 277

Rigaut F. et al., 2014, MNRAS, 437, 2361

Rocca A., Roddier F., Vernin J., 1974, JOSA, 64, 1000

Sarazin M., Roddier F., 1990, A&A, 227, 294

Saxenhuber D., Auzinger G., Le Louarn M., Helin T., 2017, Applied Optics, 56, 2621

Stone J., Hu P., Mills S., Ma S., 1994, JOSA A, 11, 347

Tallon M., Foy R., 1990, A&A, 235, 549

Tokovinin A., 2003, JOSA A, 20, 686

Tokovinin A., 2004, PASP, 116, 941

Tokovinin A., Kornilov V., Shatsky N., Voziakova O., 2003, MNRAS, 343, 891

Vidal F., Gendron E., Rousset G., 2010, JOSA A, 27, A253

Wilson R. W., 2002, MNRAS, 337, 103

Zhu X., Kahn J. M., 2002, IEEE Trans. Comm., 50, 1293

This paper has been typeset from a TEX/LATEX file prepared by the author.